Supplementary Information (SI) for Chemical Communications.

Supporting Information

Promoting Reactant Accumulation at Solid–Liquid Interfaces through Microstrain-Defect Engineering in Overall Water Splitting

Krishankant, Alok Kumar†, Rohit Bisht†, Rekha Rani, Gyan Prakash Chauhan, Payal Thakur, Chandan Bera,* and Vivek Bagchi*

Institute of Nano Science and Technology, Sector-81, Knowledge City, Sahibzada Ajit Singh Nagar, Punjab, 140306, INDIA

† Represent Equal Contribution Second Authorship

*Corresponding Author: bagchiv@inst.ac.in, vivekbagchi@gmail.com ; chandan@inst.ac.in

Table of Content

	resistance (R_{CT})

S1. Experimental Section

Chemical and Reagents

Cobalt nitrate hexahydrate ($Co(NO_3)_2.6H_2O$), ferric nitrate nonahydrate ($Fe(NO_3)_3.9H_2O$), urea ($CO(NH_2)_2$), ammonium fluoride (NH_4F), potassium hydroxide (KOH), sodium dihydrogen phosphate (NaH_2PO_4), and, sulfur powder (S) were purchased from CDH chemicals (central drug house) and used with further treatment. All solutions were prepared in the deionized water (D.I).

Synthesis of CoFeLDH by Microwave Digestor Method

The appropriate amount of Co and Fe in salt form was dissolved into 30 mL D.I. followed by the addition of 10 mmol urea and 5 mmol NH_4F. The mixture was stirred for a few minutes and then transferred into the sealed falcons. The program in the oven was set for 1 hour for heating at 160^o C. The brown colour precipitates were collected after the oven gets cooled. The material was centrifuged and washed with ethanol several times.

Synthesis of CoFePS

The 500 mg of CoFeLDH was put downstream and mixed S/P source were placed upstream, and the crucible boat was heated at 350^o C for 100 min, in the inert atmosphere of N_2. The black-coloured CoFePS was collected after phospho-vulcanization of CoFeLDH. The CoFeP was prepared with the same method by just avoiding the addition of an S source.

Electrochemical Measurements

All the electrochemical measurements were performed in 1 M KOH (pH = 13.8) employing the conventional three-electrode setup. The working electrode was prepared by drop-casting catalyst ink on a graphitic sheet. The catalyst ink was prepared by the addition of 5 mg of catalyst into 250 µL of ethanol, 240 µL water, and 10 µL of Nafion binder followed by ultra-sonication for 2 hours. The reference and counter electrode were used as Ag/AgCl (3M KCl) and graphite rod (2mm). The applied potential was converted into the reversible hydrogen electrode potential by formula:

$$E_{RHE} = E_{Cell} + E_{Ag/AgCl} + 0.059{*}pH \Rightarrow E_{Cell} + 0.197 + 0.826 \Rightarrow E_{Cell} + 1.023$$

The linear sweep voltammetry was employed to assess the electrochemical activity towards water splitting catalysis at the possible lower scan rate to avoid side reactions. The Tafel slope was further calculated by equation to evaluate the reaction kinetics: $\eta = a + b \log|j|$, where η, a, b, and j, represent overpotential, tafel constant, tafel slope, and current density. The double layer capacitance is also a vital factor in studying the intrinsic activity of the catalyst; thus, the CV was taken at multiple scan rates in the non-faradic regions and a graph was plotted between Δj ($j_{cathodic} - j_{anodic}$) vs. scan rate to obtain a slope, which represents the double layer capacitance (C_{dl}). Electrochemical impedance spectroscopy was performed to calculate the charge transfer resistance, Warburg diffusion coefficient, and diffusion coefficient. The details are given in the manuscript. The stability experiment was performed via the chronoamperometric technique.

Physical Characterization

The CoFePS and other supplementary materials were primarily characterized by PXRD by RIGAKU PXRD in the range of 10-70°, with the increment of 10°/min rate. To verify the morphology and claim the self-templating fact, FESEM (field emission scanning electron microscopy) was performed via JEOL (JSM 17-300) and TEM (Transmission electron microscopy) via JEOL-2100 at 200 kV. The XPS (XPS, ECSA:220-IXL) was further involved to understand the valence states and elements present on the surface of the catalyst. ICP-MS (Agilent 7850) was performed to examine the leached-off metal ions in electrolyte post-stability in both no-gas and helium modes. UV-Vis-NIR (Agilent Cary) was employed to record the absorbance of catalysts, which helped in calculating the band gap by Tauc plot. The AFM images were recorded on an Oxford Instrument Scanning Probe Microscope and the images were analysed using the Gwydion software. The tip used was of Pt with a work function of ~5.1 eV.

S2. COMSOL Modelling

The finite element method (FEM) model was constructed with COMSOL Multiphysics as stationary. To simplify the model, we used 2D axisymmetric modeling with distinct electrical conductivity because the catalytic reaction occurred mainly on the surface. The model material was nanofelt like structure in a circular vicinity of bulk electrolyte with a geometric dimension of 1 µm ×3 µm (width × height) electrode's surface. The "transient dilute species" and "electrostatics" module was used to examine the electric field when the electrode was under a 0.5 V potential. The electric field (E) was computed as the negative gradient of the electric potential as follows:

$$E = -\nabla V \qquad (1)$$

Additionally, Ohm's law was used to correlate the electric field to current density (J),

$$J = \sigma E \qquad (2)$$

in which σ is the electrical conductivity. The electrical conductivity of the two electrode was measured by CAFM (conductive atomic force microscopy) found to be 0.2 and 0.004 S m^{-1}, for CoFePS and CoFeLDH, respectively, while the electrolyte conductivity was assumed to be 10 S m^{-1}.

In the diffuse layer, the cations and anions freely diffuse in the electrolyte, and form concentration gradients towards and away from the electrode surface. The "Transport of diluted species" module was used to analyze the hydroxide ion (OH^-) density in the electrical double layer. The diffusion coefficients of the K^+, OH^-, and H^+ ions in H_2O were taken to be 2.14×10^{-9}, 7.02×10^{-9}, and 7.10×10^{-9} $m^2\ s^{-1}$, respectively. Conventional triangular meshes were used for all simulations and the meshes were set to the densest grid around the electrode.

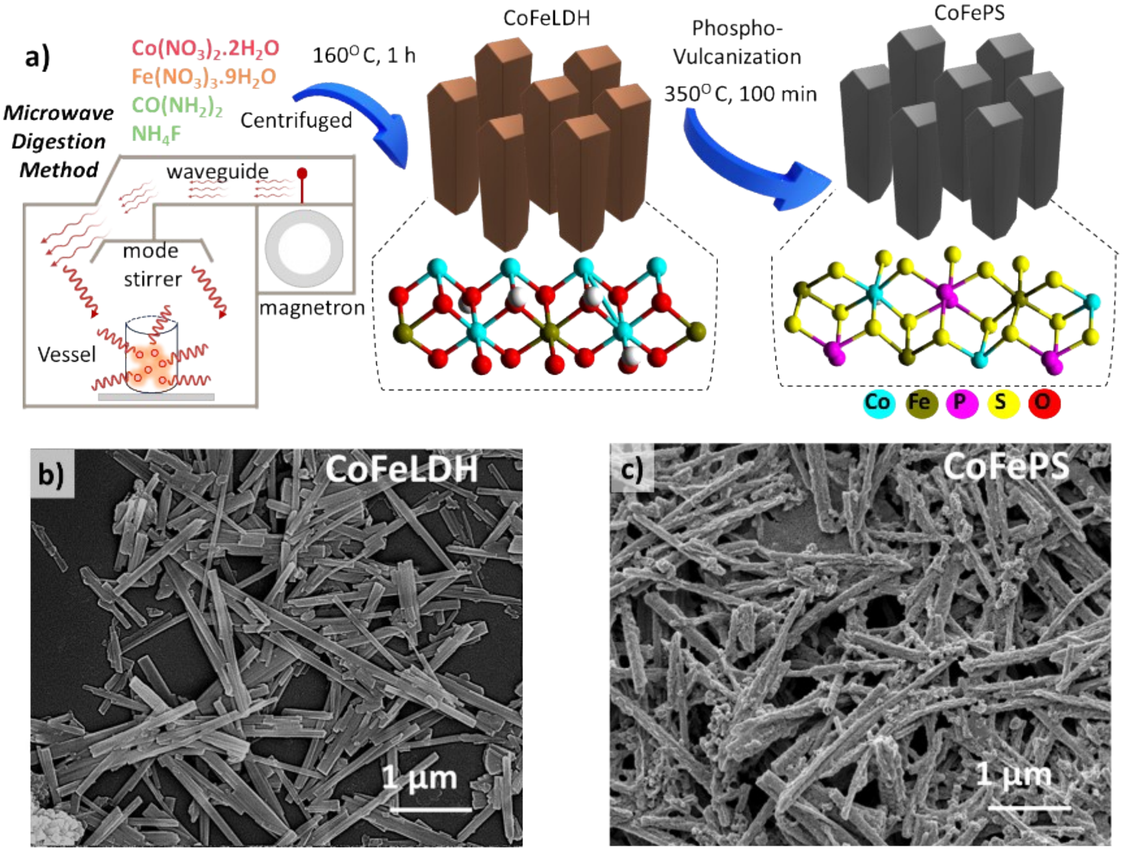

Fig. S1. a) Synthesis illustration of CoFePS, FESEM micrographs of b) CoFeLDH and c) CoFePS.

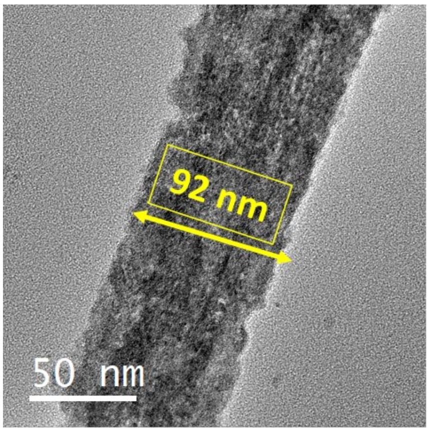

Fig. S2. TEM nanograph of CoFePS at 50 nm, indicating a width of 92 nm.

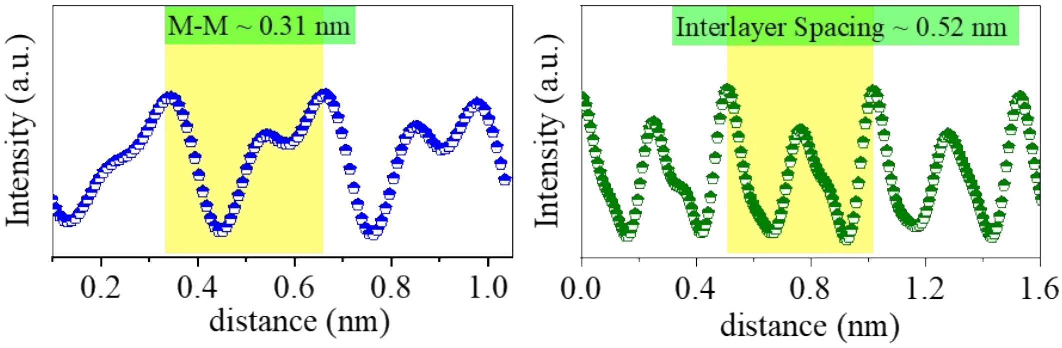

Fig. S3. IFFT derived M-M distance and interlayer spacing of CoFePS.

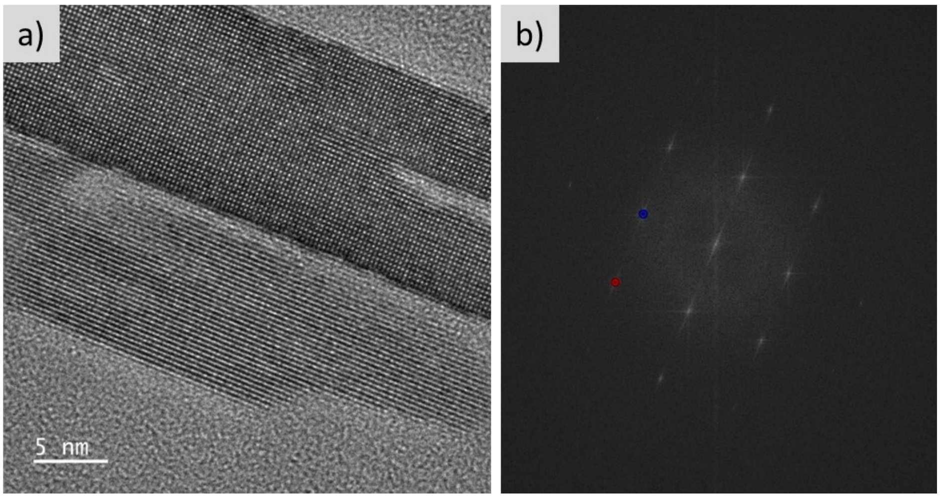

Fig. S4. TEM analysis of CoFeLDH, a) HR-TEM and b) corresponding FFT pattern (strain calculated between marked planes).

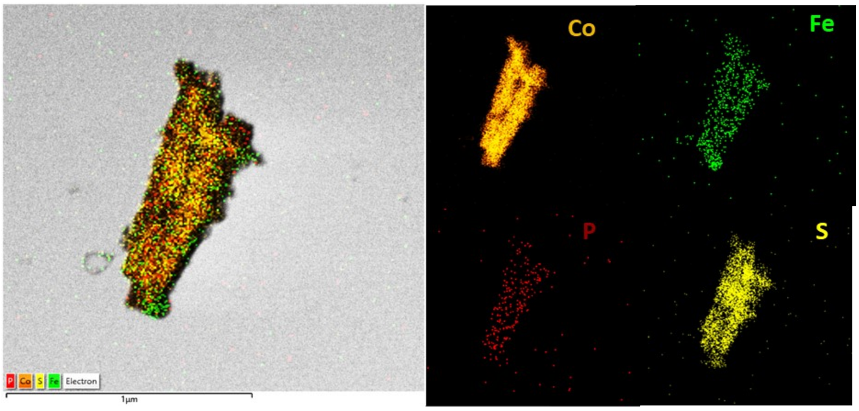

Fig. S5. Elemental mapping of CoFePS for Co, Fe, P and S, respectively.

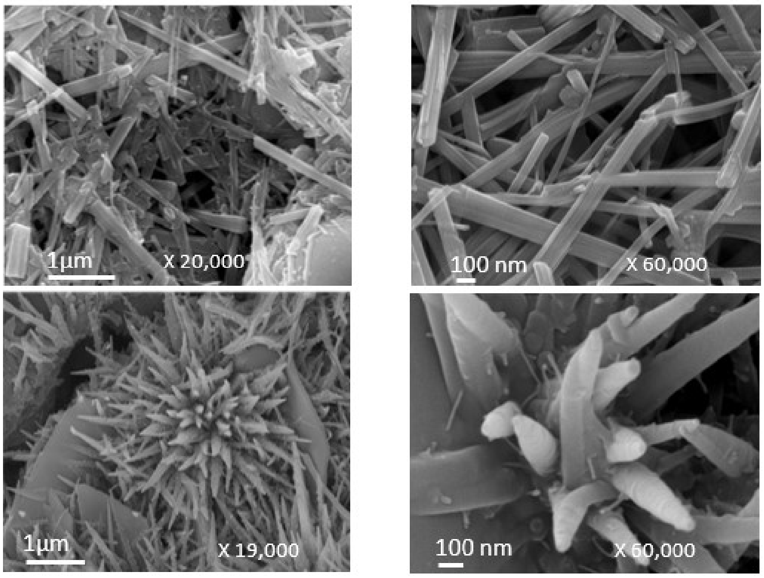

Fig. S6. FESEM micrographs of CoFeLDH (TOP) and CoFeP (BOTTOM) at different microscopic resolution.

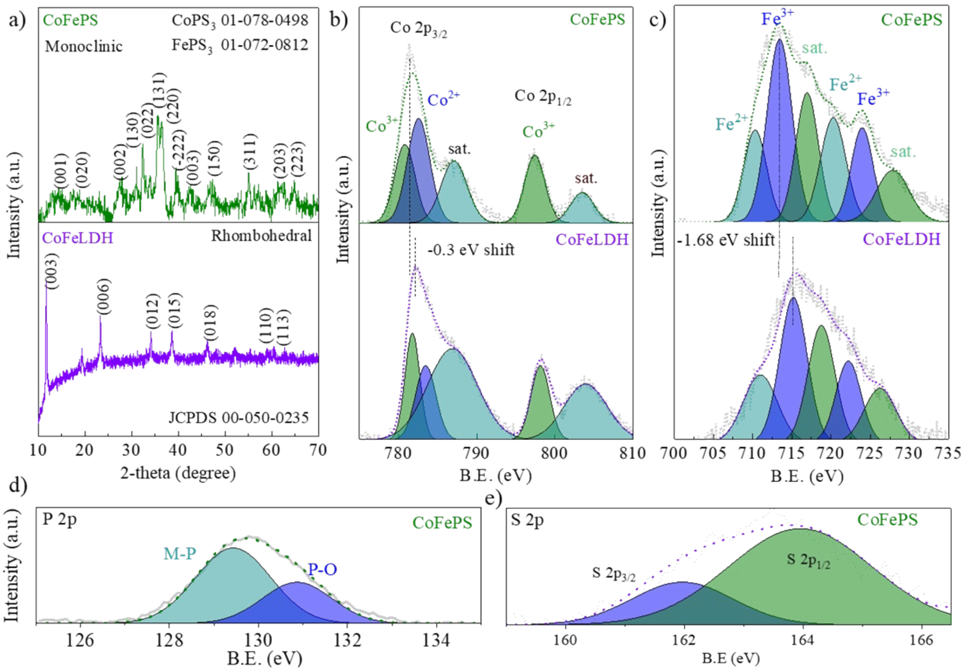

Fig. S7. Physical characterization of CoFePS, a) PXRD, and XPS of b) Co 2p, c) Fe 2p, d) P 2p, e) S 2p, respectively.

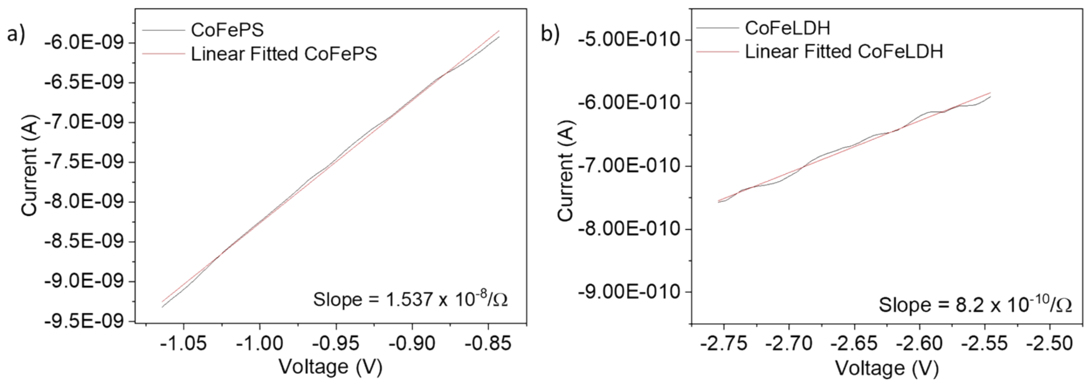

Fig. S8. Conductive Atomic Force Microscopy (CAFM) for electrical conductivity measurements at the surface of a) CoFePS, and b) CoFeLDH

CAFM was performed to obtain the I-V curve. The calculations for electrical conductivity evaluation is given below:

More specifically,

For CoFePS

Slope = 1.537 x 10^{-8} / ohm

R = 1/Slope = 1/1.537 x 10^{-8} (ohm)

Now we have,

σ = L/RA (Equation 1)

here, σ, L, R, and A, represents electrical conductivity, thickness, resistance, and effective cross-sectional area, respectively.

For the AFM tip the radius is 35 nm, which resulted in the A (Area) of 3850 nm^2.

Putting all values if equation 1.

σ = 0.2 S/m

Similarly, for CoFeLDH, the slope is 8.2 x 10^{-10} / ohm

Which led to the σ of 0.004 S/m.

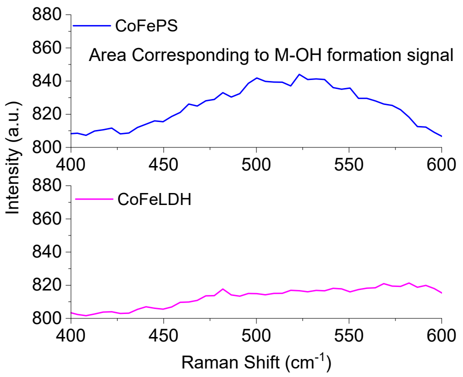

Fig. S9. Raman spectra for CoFePS and CoFeLDH for tracking M-OH formation

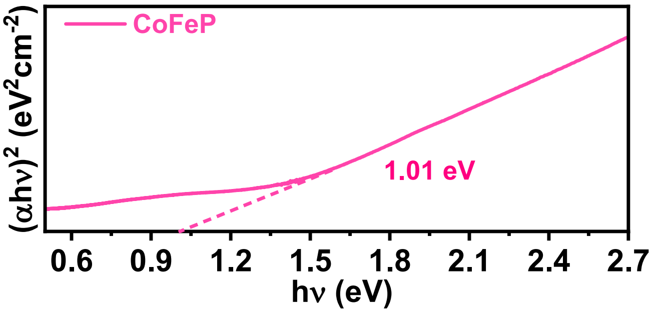

Fig. S10 Tauc plot of CoFeP.

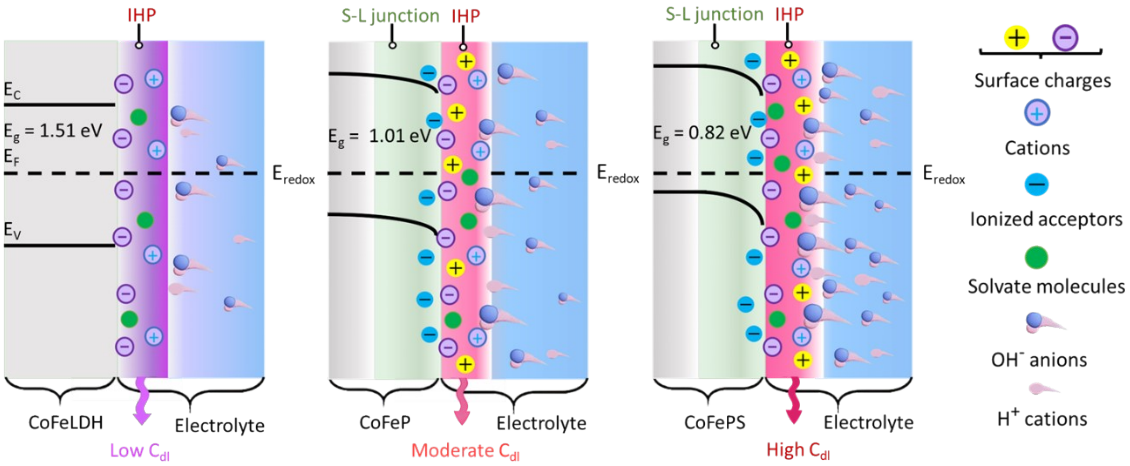

Fig. S11. Schematic representation of optimization and formation of S-L junction with different electronic properties of CoFeLDH, CoFeP, and CoFePS.

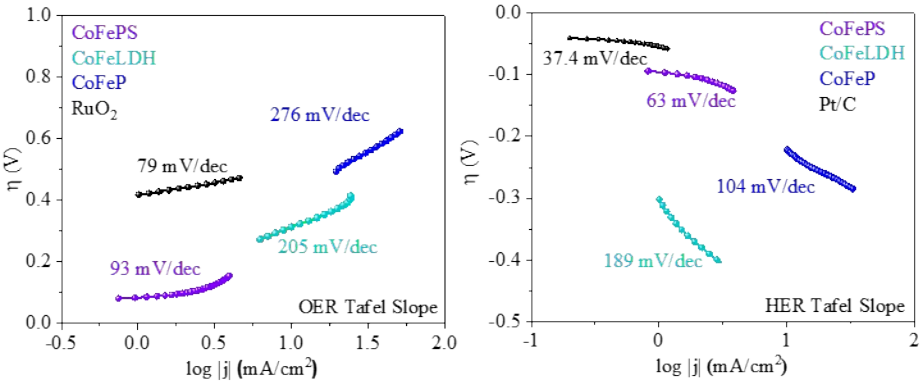

Fig. S12. Tafel Slope analysis for OER (left) and HER (right).

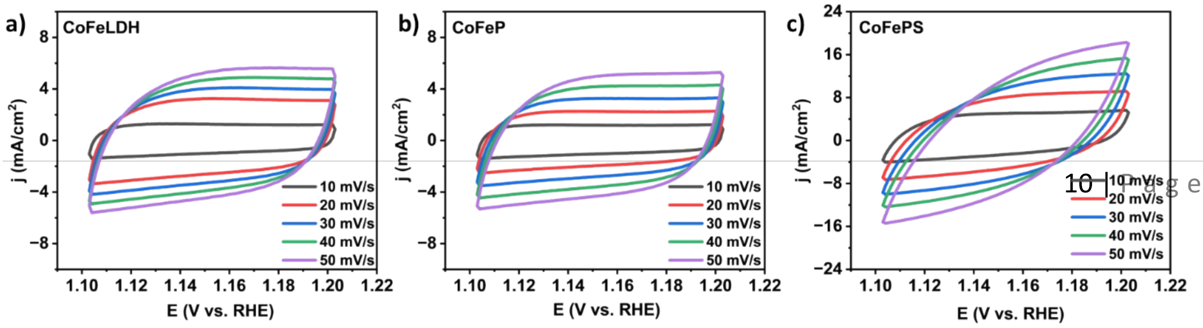

Fig. S13. Cyclic voltammetry curve of a) CoFeLDH, b) CoFeP, and c) CoFePS, at different scan rates, Respectively.

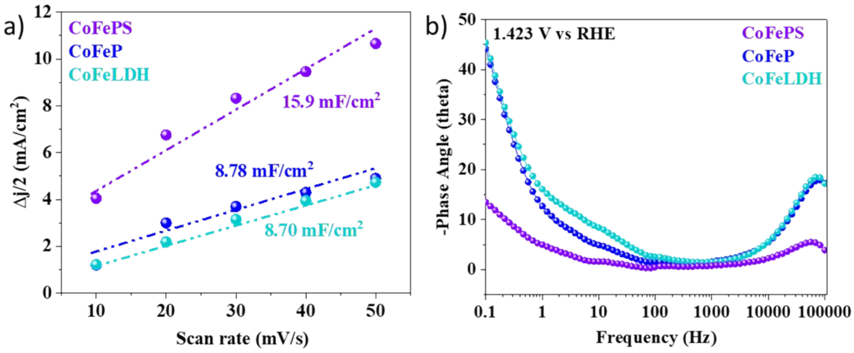

Fig. S14. Intrinsic activity evaluation with a) C_{dl} plot and b) EIS Bode's plot for CoFePS, CoFeP, and CoFeLDH, respectively.

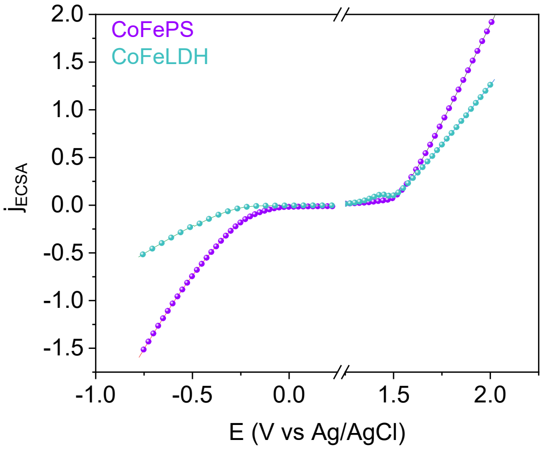

Fig. S15. ECSA normalized LSV of CoFePS and CoFeLDH.

To distinguish between the effects of increased surface area and enhanced intrinsic activity, the ECSA-normalized specific activity for both HER and OER was calculated. While CoFePS exhibits a higher ECSA of 397.5 cm^2 compared to CoFeLDH (217.5 cm^2), the ECSA-normalized polarization curves demonstrate that CoFePS still maintains a significantly better electrochemical activity. This confirms that the performance enhancement is not solely due to increased site exposure from the nanofelt morphology, but stems fundamentally from the improved intrinsic activity per site induced by microstrain-defect engineering.

Table S1: Comparison of recently reported transition metal based electrocatalysts for HER in 1 M KOH:

Catalyst	η_{10} (mV)	Stability (h)	References
This Work	56	40	-
Co_3S_4-MoS_2	117	10	1

$Co_{0.5}Fe_{0.5}$-LDH	365	8	2
Pt-NiCo LDO	92	105	3
Ru_{SA}-NiS_2-FeS_2	57	50	4
CoFeP/CoP-400	78	12	5
CoFe-LDH@CoP/NF	68	80	6
($NiCo_{16-x}P_6$)	88	10	7
P−$NiCuFe_{0.06}$−LDH	71	120	8
H-COS_X@NiFe LDH/NF	95	100	9
NiFe LDH-Ni-S/NF	94	20	10
Fe-CoS_2	217	25	11
P-$CoNi_2S_4$	135	40	12
Co_9S_8@Co_3O_4/NF	130	50	13
CoMoNiS-NF-31	103	24	14
Super-Co_3S_4/P-WS_2/Co_9S_8	58	24	15
FeCo-FeCoP@C@NCCs	91	11	16
CoP@FeCoP/NC	141	20	17
CoFeP @ C	181	20	18

Table S2: Comparison of recently reported transition metal based electrocatalysts for OER in 1 M KOH:

Catalyst	**η_{10} (mV)**	**Stability (h)**	**References**
This Work	145	40	-
CoP/CoFeP	266	150	19
CoFe-250	230	30	20
CoFe-LDH@CoP/NF	238	80	6
NiFe-LDH/ Ni_4Mo	192.5	60	21
O-Co_2P/CuO NWs	270	30	22
$Ni_{0.75}V_{0.25}$ LDH	200	100	23
$Co_{0.5}Fe_{0.5}$-LDH	270	10	2
$(NiFeCoMn)_3S_4$	286	48	24
NiCoFe HO@NiCo-LDH	278	11	25
Fe-Co_3O_4	262	50	26
CoFeLDH@NiSe	127	24	27
CoFe-LDH@CoP/NF	238	80	6
NiFeCoP-1/CC	249	12	28
CoNi/NC-YS	292	24	29
NMO-30M	260	162	30
CoO@NiO	270	24	31
CoP-InNC@CNT	270	20	32
NiO-Ni_3Se_4/MXene	260	24	33

Table S3: Comparison of overall cell potential of CoFePS||CoFePS with another Co-Fe based electrocatalyst.

Catalyst	Cell Potential @10 mA/cm^2	Stability (h)	Reference
CoFePS	1.436	200	This work
J-CoFe-CFP	1.56	10	[34]
$Fe_{0.5}CoNi_{0.5}P$	1.52	70	[35]
Co_7Fe_3/Co	1.50	100	[36]
A-$Co_{60}Fe_{1.1}V$	1.54	40	[37]
Co_2P-Fe_2P	1.45	50	[38]
$Fe_{0.4}Co_{0.3}Ni_{0.3}$-1.8	1.62	50	[39]
m-CFO IO	1.55	50	[40]
$Co(OH)_2/Fe_7Se_8$	1.62	20	[41]
Co3Fe/Ce0.025	1.70	25	[42]
$CeCO_3OH$/Ce-CoFe LDH	1.61	80	[43]
V_P-Fe-CoP	1.63	100	[44]

Post OER-FESEM

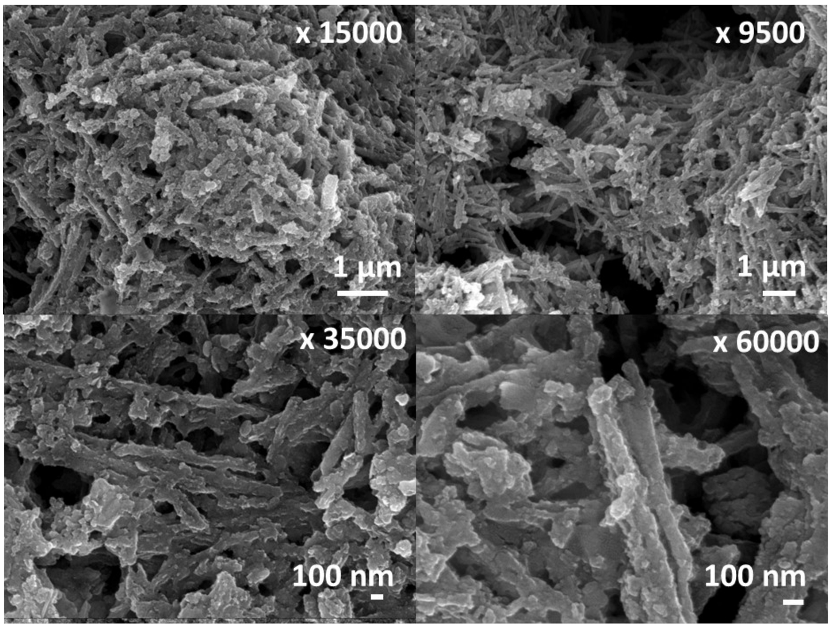

Fig. S16. Post-OER FESEM of CoFePS at different microscopic resolution.

During OER, the CoFePS shows no appreciable change in the morphology, as the nanofelts seems intact. However, the growth of tiny nanosheets over these nanofelts indicates the formation of active surface during OER.

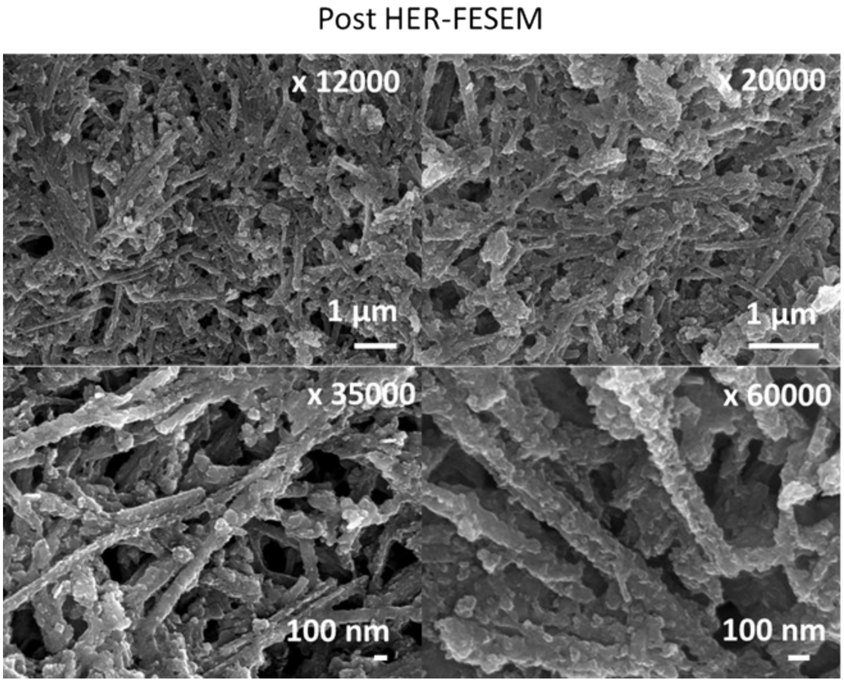

Fig. S17. Post-HER FESEM of CoFePS at different microscopic resolution.

Similar to post-OER morphology, the post-HER morphology indicates intact morphology for CoFePS.

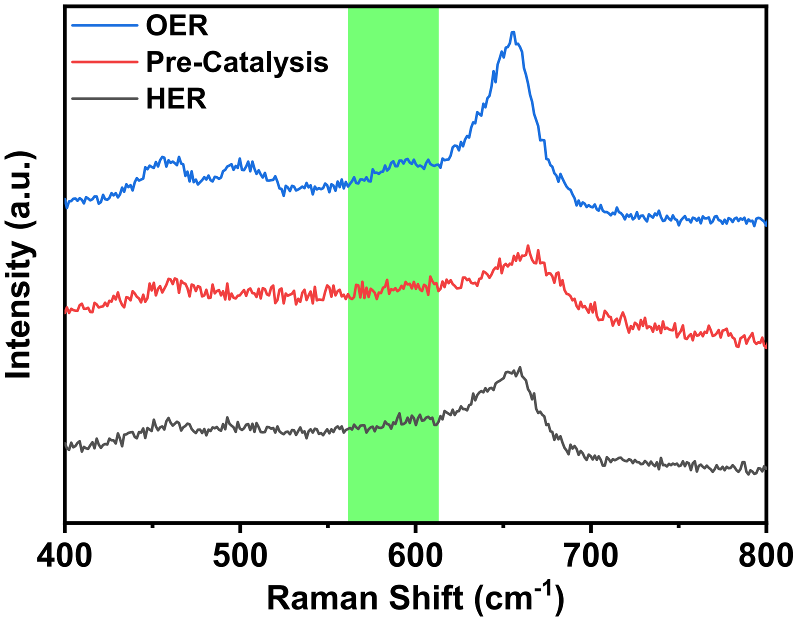

Fig.S18. Post HER/OER Raman Spectra of CoFePS.

Post-Electro Raman spectra indicate the intact structure post-HER, however, post-OER there is appreciable rise in peaks near between 420-530 cm^{-1} corresponding to the M-O and M-OH bond stretching.

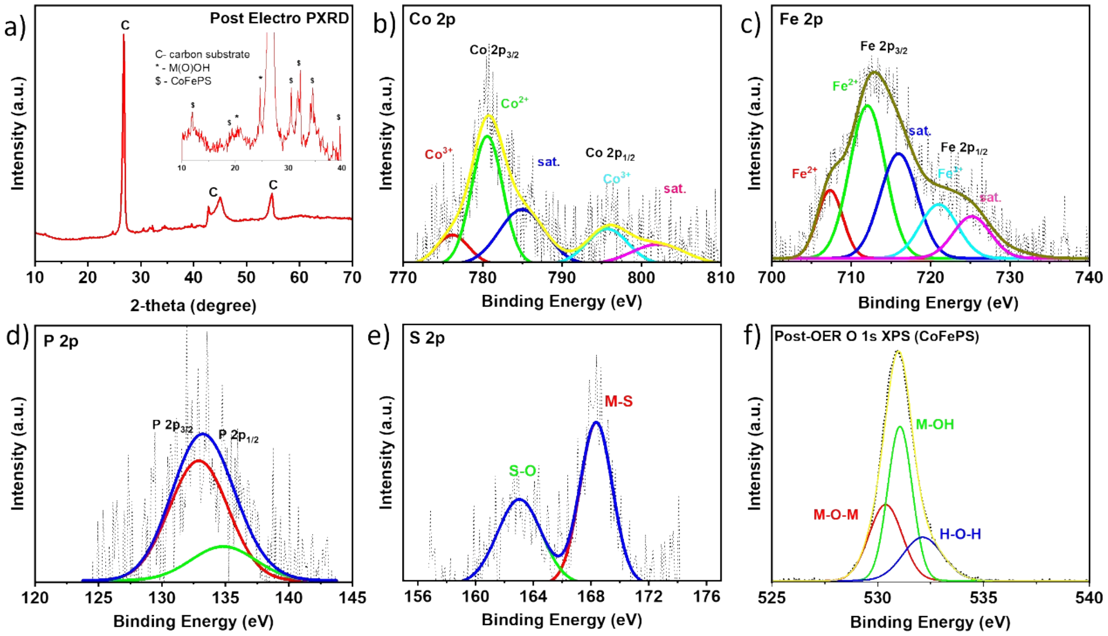

Fig.S19. Post -OER physical characterization of CoFePS, a) PXRD, and XPS of b) Co 2p, c) Fe 2p, d) P 2p,

e) S 2p, and f) O1s elements.

Fig. S19a displays PXRD pattern for post-OER CoFePS electrode, where the peaks corresponding to * mark indicates M(O)OH surface (M= Co/Fe), with few intact peaks for CoFePS. Furthermore, the XPS spectra suggests the Low leaching percentage of Co and Fe, in both HER and OER, suggests efficient mechanical strength of CoFePS, making it suitable prolonged operations.

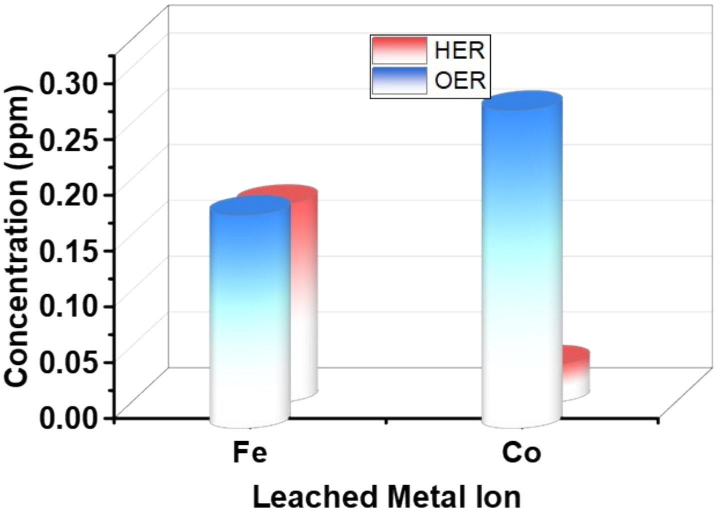

Fig.S20. Post HER/OER electrolyte analysis for metal ion leaching by ICP-MS.

The leaching amount of Co was found to be 0.28 and 0.03 ppm, post-OER and HER respectively. In addition, the leaching amount of Fe was determined as 0.19 and 0.17 ppm, respectively. The minimal leaching amount suggesting excellent mechanical strength.

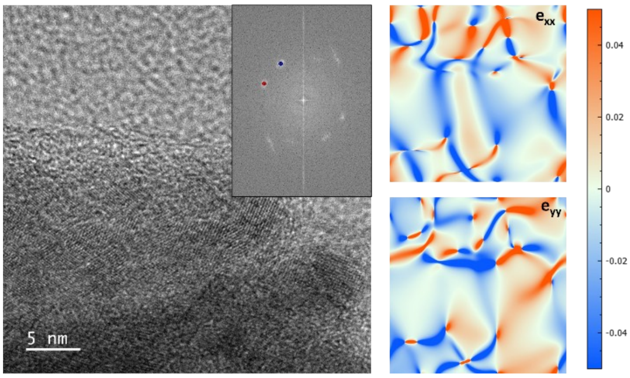

Fig. S21. GPA Strain analysis of CoFePS post-stability experiment.

GPA analysis revealed an intact microstrain in CoFePS lattice indicating robust mechanical strength of crystal structure.

S3. Computational Details

The electronic energy of the simulated crystal structure was calculated by optimized the geometry of the structures. Further the Gibbs free energy was evaluated via employing specific formulas for HER and OER, respectively. The supercell was transformed into a 2x2x1 matrix with a vacuum of 15 Å in the c-axis direction to avoid periodic interaction.

The mechanism of OER in alkaline medium is given below:

- $OH^- + M^* \rightarrow M\text{-}OH^* + e^-$
- $OH^* + OH^- \rightarrow M\text{-}O^* + H_2O(l) + e^-$
- $OH^- + M\text{-}O^* \rightarrow M\text{-}OOH^* + e^-$
- $OH^- + M\text{-}OOH^* \rightarrow O_2(g) + H_2O(l) + e^-$

Overall reaction is: $4\,OH^- \rightarrow O_2 + 2H_2O + 4e^-$

The formula's employed for the calculation of OER ΔG values are given below:

$E_{[OH]} = E(OH) - E^* - (E_{H2O} - ½\,E_{H2})$

$E_{[O]} = [E(O) - E^* - (E_{H2O} - ½\,E_{H2})]$

$E_{[OOH]} = [E(OOH) - E^* - (2E_{H2O} - 3/2\,E_{H2})$

Now,

$G1 = E_{[OH]}$

$G2 = E_{[O]} - E_{[OH]}$

$G3 = E_{[OOH]} - E_{[O]}$

$G4 = 4.92 - (G1 + G2 + G3)$: At equilibrium potential

$G4 = [4.92 - (G1 + G2 + G3)] - 1.23$: At 1.23 V

Similarly, for HER,

The reaction mechanism in alkaline conditions is given below:

$H_2O + M + e^- \leftrightarrows M\text{-}H_{ad} + OH^-$ (the Volmer step)

$H_2O + M\text{-}H_{ad} + e^- \leftrightarrows M + H_2 + OH^-$ (the Heyrovsky step)

Or

$2M\text{-}H_{ad} \leftrightarrows 2M + H_2$

Further the Gibbs free energy can be calculated by following equation,

$G_{[H]} = E(H^*) - E^* + 0.24$

In above equation the zero point energy, pH and other factors are neglected.

In all above equation E represents the electronic energy of the component which is given in the brackets, and G is the Gibbs free energy, and * represents the intermediates.

Table below indicates the values of electronic energies and the Gibbs free energies of the crystal structures:

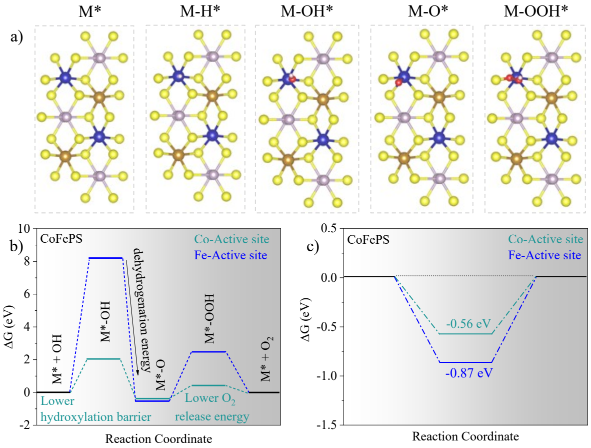

Fig S22. a) Optimized CoFePS structure and Gibbs free energy profile for b) OER and c) HER, respectively.

In Fig. S22b, the ΔG profile for OER intermediate adsorption reveals that the metal surface at the Co-active site exhibits a lower hydroxylation energy in comparison to the Fe- site. During the second step of dehydrogenation, one can observe the spontaneous process characterised by the transition from M*-OH to M*-O formation, which follows a downhill pathway. In the third step, often regarded as the rate-determining step in various Co-based catalysts, the Co-active site within the system governs the reaction by lowering the energy barrier. The minimal energy difference observed in the fourth step of O_2 release which indicates that Co serves as a more effective active site for catalysis. The potential limiting step is identified at 2.01 eV, where the M* active site experiences a hydroxylation process. This value is notably lower than the 5.08 eV observed for CoFeLDH, as discussed in our previous article.[13] In Fig. S22c, the protonation occurring over the catalytic surface of CoFePS, along with their respective metal sites, was analysed for the HER process. Notably, the Co-active site in CoFePS exhibited a ΔG value of -0.56 eV, which is optimal for HER. Consequently, the Co-site in CoFePS demonstrates activity in the adsorption process for both HER and OER, while the Fe-site contributes to the modulation of electronic arrangements within the catalyst.

Table S4: Electronic energy of simulated crystal structures and their respective Gibbs free energy

Material	***HER***	
	E (eV)	***G (eV)***
CoFeLDH	-101.67	-
CoFeLDH (On Co)	-105.83	-3.92
CoFeLDH (On Fe)	-103.83	-2.16
CoFePS	-114.84	
CoFePS (On Co)	-115.65	-0.57
CoFePS (On Fe)	-115.94	-0.86
	OER on Co site	
CoFePS-OH	-123.04	2.05
CoFePS-O	-120.91	-2.49
CoFePS-OOH	-130.3	0.86
CoFePS + O_2	-	-0.41
	OER on Fe site	
CoFePS-OH	-116.88	8.21
CoFePS-O	-120.91	-8.65
CoFePS-OOH	-128.25	2.91
CoFePS + O_2	-	-2.46

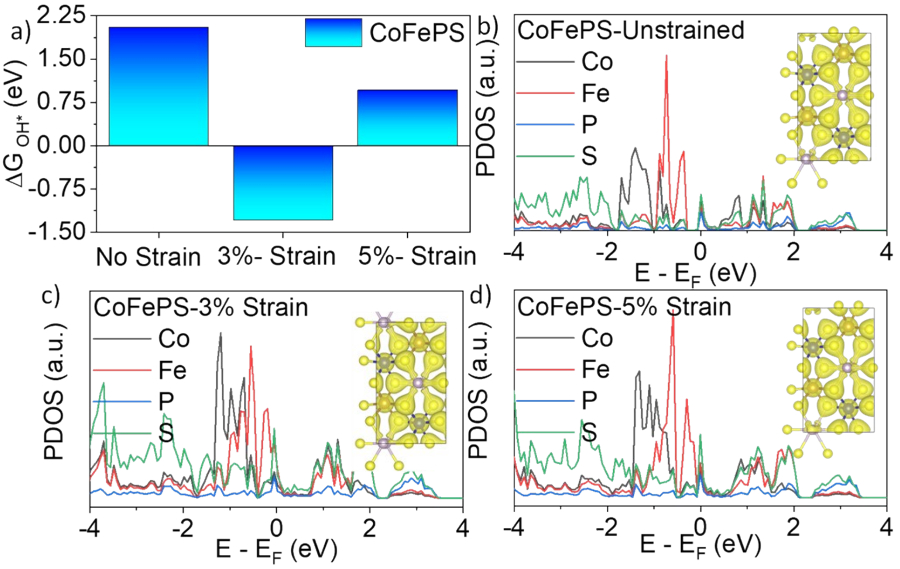

Fig. S23. a) Gibbs free energy of OH* adsorption comparison with strained and unstrained CoFePS. PDOS of b) CoFePS-Unstrained, c) 3% Strain, and d) 5% Strain, with inset charge density distribution.

References

1 Y.-Q. He, H.-M. Xu, J.-D. Zhang, D. Zheng, G. Zhang, X.-Z. Fan, H. Ou-Yang, Y.-Q. Liu, A.-C. Lv, J.-W. Zhao, C.-W. Shi and S.-K. Han, *Angewandte Chemie International Edition*, 2025, **64**, e202414720.

2 S. Shankar Naik, J. Theerthagiri, F. S. Nogueira, S. J. Lee, A. Min, G.-A. Kim, G. Maia, L. M. C. Pinto and M. Y. Choi, *ACS Catal.*, 2023, **13**, 1477–1491.

3 Y. Tian, Y. Luo, T. Wu, X. Quan, W. Li, G. Wei, M. Bayati, Q. Wu, Y. Fu and M. Wen, *Advanced Functional Materials*, 2024, **34**, 2405919.

4 R. B. Ghising, U. N. Pan, M. R. Kandel, P. P. Dhakal, S. Sidra, D. H. Kim, N. H. Kim and J. H. Lee, *J. Mater. Chem. A*, 2024, **12**, 3489–3500.

5 L. Tan, R. He, A. Shi, L. Xue, Y. Wang, H. Li and X. Song, *Inorg. Chem.*, 2023, **62**, 9964–9970.

6 Z. Song, H. Xuan, S. Liu, L. Meng, J. Wang, X. Liang, Y. Li, Z. Han and P. Han, *Chemical Engineering Science*, 2024, **294**, 120100.

7 Y. Zhao, J. Zhang, Y. Xie, B. Sun, J. Jiang, W.-J. Jiang, S. Xi, H. Y. Yang, K. Yan, S. Wang, X. Guo, P. Li, Z. Han, X. Lu, H. Liu and G. Wang, *Nano Lett.*, 2021, **21**, 823–832.

8 Y. Zhang, S. Lee, S. Jeong, E. Son, J. M. Baik, Y.-K. Han and H. Park, *Advanced Functional Materials*, 2024, **34**, 2309250.

9 Y. J. Lee and S.-K. Park, *Small*, 2022, **18**, 2200586.

10 X. Zhang, Y. Xue, Q. Yan, K. Zhu, K. Ye, J. Yan, D. Cao, X. Huang and G. Wang, *Materials Today Energy*, 2021, **21**, 100741.

11 S. Qiang, Z. Li, S. He, H. Zhou, Y. Zhang, X. Cao, A. Yuan, J. Zou, J. Wu and Y. Qiao, *Nano Energy*, 2025, **134**, 110564.

12 X. F. Lu, S. L. Zhang, W. L. Sim, S. Gao and X. W. (David) Lou, *Angewandte Chemie International Edition*, 2021, **60**, 22885–22891.

13 X. Wang, Y. He, X. Han, J. Zhao, L. Li, J. Zhang, C. Zhong, Y. Deng and W. Hu, *Nano Res.*, 2022, **15**, 1246–1253.

14 Y. Yang, H. Yao, Z. Yu, S. M. Islam, H. He, M. Yuan, Y. Yue, K. Xu, W. Hao, G. Sun, H. Li, S. Ma, P. Zapol and M. G. Kanatzidis, *J. Am. Chem. Soc.*, 2019, **141**, 10417–10430.

15 H. Wang, J. Xu, Q. Zhang, S. Hu, W. Zhou, H. Liu and X. Wang, *Advanced Functional Materials*, 2022, **32**, 2112362.

16 Y. Li, S. Li, J. Hu, Y. Zhang, Y. Du, X. Han, X. Liu and P. Xu, *Journal of Energy Chemistry*, 2021, **53**, 1–8.

17 J. Shi, F. Qiu, W. Yuan, M. Guo and Z.-H. Lu, *Chemical Engineering Journal*, 2021, **403**, 126312.

18 Y. Deng, Y. Cao, Y. Xia, X. Xi, Y. Wang, W. Jiang, D. Yang, A. Dong and T. Li, *Advanced Energy Materials*, 2022, **12**, 2202394.

19 L. Fu, J. Zhou, Z. Zhou, B. Xiao, N. Khaorapapong, Y. Kang, K. Wu and Y. Yamauchi, *ACS Nano*, 2023, **17**, 22744–22754.

20 Q. Zhang, M. Sun, J. Zhu, S. Yang, L. Chen, X. Yang, P. Wang, K. Li, F. Xue, Y. Lu, J. Zhang and P. Zhao, *Chemical Engineering Journal*, 2022, **432**, 134275.

21 F. Wu, F. Tian, M. Li, S. Geng, L. Qiu, L. He, L. Li, Z. Chen, Y. Yu, W. Yang and Y. Hou, *Angewandte Chemie International Edition*, 2025, **64**, e202413250.

22 T. L. Luyen Doan, D. T. Tran, D. C. Nguyen, H. Tuan Le, N. H. Kim and J. H. Lee, *Applied Catalysis B: Environmental*, 2020, **261**, 118268.

23 H. S. Chavan, C. H. Lee, A. I. Inamdar, J. Han, S. Park, S. Cho, N. K. Shreshta, S. U. Lee, B. Hou, H. Im and H. Kim, *ACS Catal.*, 2022, **12**, 3821–3831.

24 L. Wu, X. Shen, Z. Ji, J. Yuan, S. Yang, G. Zhu, L. Chen, L. Kong and H. Zhou, *Advanced Functional Materials*, 2023, **33**, 2208170.

25 Q. Niu, M. Yang, D. Luan, N. W. Li, L. Yu and X. W. (David) Lou, *Angewandte Chemie International Edition*, 2022, **61**, e202213049.

26 S. L. Zhang, B. Y. Guan, X. F. Lu, S. Xi, Y. Du and X. W. (David) Lou, *Advanced Materials*, 2020, **32**, 2002235.

27 S. M. N. Jeghan, D. Kim, Y. Lee, M. Kim and G. Lee, *Applied Catalysis B: Environmental*, 2022, **308**, 121221.
28 Z. Cai, P. Wang, J. Zhang, J. Xu, Y. Yan, A. Chen and X. Wang, *Journal of Alloys and Compounds*, 2023, **933**, 167743.
29 G. Hou, X. Jia, H. Kang, X. Qiao, Y. Liu, Y. Li, X. Wu and W. Qin, *Applied Catalysis B: Environmental*, 2022, **315**, 121551.
30 J. Zhu, J. Qian, X. Peng, B. Xia and D. Gao, *Nano-Micro Lett.*, 2023, **15**, 30.
31 J. Liu, M. Zheng, J. Li, Y. Yuan, C. Li, S. Zhang, L. Yang, Z. Bai and J. Lu, *Advanced Functional Materials*, 2023, **33**, 2209753.
32 L. Yan, J. Liang, D. Song, X. Li and H. Li, *Advanced Functional Materials*, 2024, **34**, 2308345.
33 L. Chai, Z. Hu, X. Wang, Y. Xu, L. Zhang, T.-T. Li, Y. Hu, J. Qian and S. Huang, *Advanced Science*, 2020, **7**, 1903195.
34 X. Li, H. Zhang, X. Li, Q. Hu, C. Deng, X. Jiang, H. Yang and C. He, *Nano Res.*, 2023, **16**, 2245–2251.
35 L. Kumar, B. Antil, A. Kumar, M. R. Das, O. López-Estrada, S. Siahrostami and S. Deka, *ACS Appl. Mater. Interfaces*, 2023, **15**, 54446–54457.
36 X. Wang, X. Xu, Y. Nie, R. Wang and J. Zou, *Advanced Science*, 2023, **10**, 2301961.
37 L. Ge, H. Yang, J. Guan, B. Ouyang, Q. Yu, H. Li and Y. Deng, *Inorg. Chem.*, 2023, **62**, 15664–15672.
38 J.-Z. Zhang, Z. Zhang, H.-B. Zhang, Y. Mei, F. Zhang, P.-X. Hou, C. Liu, H.-M. Cheng and J.-C. Li, *Nano Lett.*, 2023, **23**, 8331–8338.
39 Y. Chen, L. Yang, C. Li, Y. Wu, X. Lv, H. Wang and J. Qu, *ENERGY & ENVIRONMENTAL MATERIALS*, 2024, **7**, e12590.
40 T. H. T. Nguyen, Z. Zarkua, C. V. Chinnappa, W. Hu, S. P. Sree, D. Grandjean, D. Pant and E. Janssens, *Nanoscale*, 2023, **15**, 10306–10318.
41 C. Gong, L. Zhao, D. Li, X. He, H. Chen, X. Du, D. Wang, W. Fang, X. Zeng and W. Li, *Chemical Engineering Journal*, 2023, **466**, 143124.
42 X.-Z. Song, T. Zhang, Y.-H. Zhao, J.-C. Ni, Y. Pan, Z. Tan and X.-F. Wang, *Inorg. Chem.*, 2023, **62**, 8347–8356.
43 J. Tang, J. Hu, X. Chen, B. Yang, K. Zhang, Y. Li, Y. Yao and S. Zhang, *Fuel*, 2024, **365**, 131128.
44 R. Na, K. Min, M. Kim, S. Min and S.-H. Baeck, *Advanced Sustainable Systems*, 2023, **7**, 2300130.